Optical waveguides and beam splitters using low-loss aluminum oxide for visible-wavelength photonics applications

Yamaguchi, Takuto; Fushimi, Naoki; Hida, Masaharu; Hosoi, Hirokazu; Ohtomo, Manabu; Miyatake, Tetsuya; Miyahara, Shoichi; Miyazawa, Toshiyuki; Kawaguchi, Kenichi; Ishihara, Ryoichi

DOI
10.35848/1347-4065/adb166

Publication date
2025

Document Version
Final published version

Published in
Japanese Journal of Applied Physics, Part 1: Regular Papers and Short Notes and Review Papers

Japanese Journal of
Applied Physics

REGULAR PAPER

Optical waveguides and beam splitters using low-loss aluminum oxide for visible-wavelength photonics applications

Japanese Journal of Applied Physics **64**, 02SP32 (2025) **REGULAR PAPER**
https://doi.org/**10.35848/1347-4065/adb166**

Optical waveguides and beam splitters using low-loss aluminum oxide for visible-wavelength photonics applications

Takuto Yamaguchi[1*], Naoki Fushimi[1], Masaharu Hida[1], Hirokazu Hosoi[1], Manabu Ohtomo[1], Tetsuya Miyatake[1], Shoichi Miyahara[1], Toshiyuki Miyazawa[1], Kenichi Kawaguchi[1], Ryoichi Ishihara[2], and Shintaro Sato[1]

[1]*Modular Quantum Computing Project, Quantum Laboratory, Fujitsu Research, Fujitsu Limited, 10-1 Morinosato-Wakamiya, Atsugi, Kanagawa 243-0197, Japan*
[2]*QuTech, Delft University of Technology, Mekelweg 4, 2628 CD Delft, The Netherlands*

[*]E-mail: y.takuto@fujitsu.com

Received October 15, 2024; revised January 27, 2025; accepted February 2, 2025; published online February 20, 2025

Low-loss visible-light photonic circuits are crucial for high-performance photonic quantum processors. By using aluminum oxide (Al_2O_3) for its low visible-light absorption, we achieved waveguides exhibiting an exceptionally low propagation loss (1.39 dB/cm for the transverse electric mode) at red-light wavelengths. Directional coupler beam splitters fabricated using this platform exhibited good controllability of the optical splitting ratios. Furthermore, we fabricated a half beam splitter, which is an essential component of entangled photon generation in quantum optics. These results represent a significant advance toward developing low-loss photonic circuits, paving the way for improved performance in photonic quantum processors.

1. Introduction

Visible-light photonic circuits have been widely studied for their potential in diverse applications, including biosensing[1–3] and scanning displays.[4,5] The need for scalable and robust optical control is particularly critical in emerging quantum computing technologies.[6–9] The precise manipulation of visible light is essential for controlling and reading quantum information stored in systems such as diamond color centers.[6–8] The longer coherence times and higher operating temperatures of diamond color centers, compared to superconducting qubits, make them strong candidates for large-scale quantum computers. However, previous free-space and fiber-optic approaches have proven complex and difficult to scale,[10] hindering progress. This limitation has been addressed by using a novel photonic circuit architecture that interconnects multiple diamond quantum modules, each containing multiple qubits, via visible-light waveguides.[8]

Several materials, including aluminum nitride,[11–14] titanium dioxide,[15–18] tantalum pentoxide,[19–21] silicon nitride[22–30] and lithium niobate[31] are being investigated for their suitability as low-loss visible-light waveguides. Among these candidates, aluminum oxide (Al_2O_3, alumina) is particularly promising.[22,32–37] Its wide bandgap ensures high visible transparency, and its low refractive index results in a reduced refractive index contrast with the cladding, thus suppressing scattering losses[38] and effectively mitigating propagation losses. Furthermore, the versatility of alumina, which allows fabrication in single-crystal, polycrystalline, and amorphous forms,[39] offers significant potential for achieving ultra-low-loss waveguides. These combined properties make alumina a strong candidate for visible-light waveguides. However, the hardness of alumina makes microfabrication challenging,[40] resulting in few reports on waveguide fabrication and characterization. Furthermore, reports on alumina waveguides designed for hybrid integration with other materials are especially limited.[33,35] Specifically, the fabrication and characterization of alumina optical beam splitters have remained largely unexplored, although they are essential for applications such as entangled photon-pair generation and efficient optical signal routing in diamond-based quantum computing.

We successfully demonstrated SiO_2-embedded alumina waveguides and beam splitters at the International Conference on Solid State Devices and Materials (SSDM).[41] This study further extends our research by investigating non-embedded alumina waveguides, which are suitable for hybrid integrated applications with other materials. We fabricate visible-light waveguides from an alumina thin film deposited by sputtering. At a wavelength of 637 nm, corresponding to the emission wavelength from nitrogen-vacancy (NV) centers in diamond, we achieved a minimum propagation loss of 1.39 dB/cm in the transverse electric (TE) mode even without SiO_2 overcladding. Furthermore, we fabricate directional coupler-type optical beam splitters and experimentally demonstrate the tunability of the optical power splitting ratio by varying a design parameter. The generation of entangled photon pairs, particularly for quantum computing applications, relies on a half beam splitter that provides equal power splitting. We demonstrate the operation of such a device in the transverse magnetic (TM) mode. This work represents a significant advance toward realizing visible-light photonic quantum chips based on low-loss alumina photonic circuits, leveraging alumina's low visible-light absorption, a crucial element for enabling quantum computation.

2. Waveguide fabrication and optical characterization

Figure 1 illustrates the fabrication process for the alumina waveguides. An approximately 300-nm-thick alumina layer was sputter-deposited onto a silicon substrate with a 2-μm-thick thermal SiO_2 layer. A SiO_2 hard mask, approximately 600-nm thick, was subsequently deposited via plasma-enhanced chemical vapor deposition (PECVD). Following the application of a negative electron-beam (EB) resist and EB lithography to define the waveguide patterns, the SiO_2 hard mask was etched using capacitively coupled plasma reactive ion etching (CCP-RIE) with CHF_3 gas. The alumina layer was then etched using inductively coupled plasma

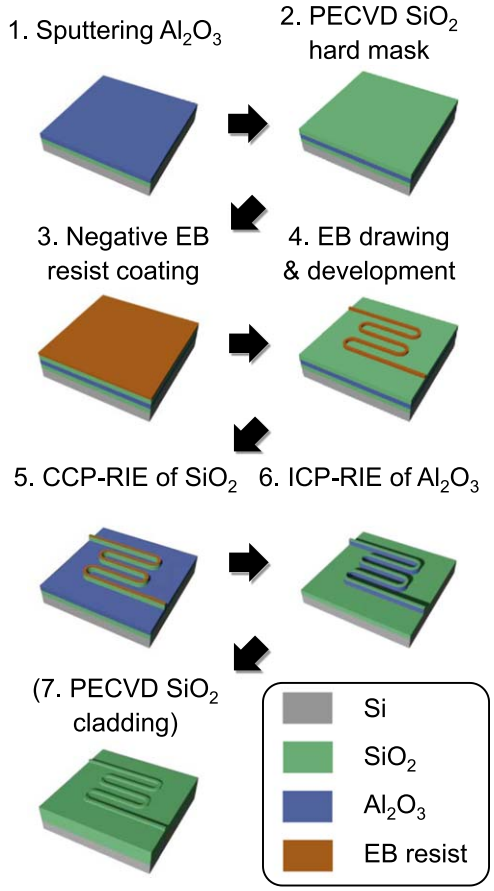

Fig. 1. Fabrication process flow for the alumina waveguides. Step 7 applies only when embedding the waveguides with SiO_2 cladding.

reactive ion etching (ICP-RIE) with a Cl_2/BCl_3 gas mixture. Successful fabrication of the waveguides required optimization of the EB resist and hard mask thickness to mitigate the challenges associated with the hardness of alumina. The approximately 2:1 selectivity ratio between SiO_2 and alumina during ICP-RIE was a key factor in determining the optimal hard mask thickness. In this study, we fabricated two types of waveguides: one with a SiO_2 cladding layer deposited by PECVD and one without cladding.

Figure 2(a) presents a cross-sectional transmission electron microscopy (TEM) image of the fabricated SiO_2-embedded alumina waveguide, confirming the successful fabrication of a channel waveguide. The refractive index of the alumina was measured to be 1.691 at 637 nm using spectroscopic ellipsometry. At the same wavelength, the refractive indices of the thermally grown and PECVD-deposited SiO_2 layers were 1.460 and 1.443, respectively. The waveguide was designed with a width W of 600 nm. Assuming a rectangular cross-section for the 293-nm-thick channel waveguides, this width should have satisfied the single-mode condition ($W \leq 650$ nm) based on the refractive index values described above. However, both CCP and ICP-RIE etching processes exhibited a reduced etch rate near the mask edge, leading to waveguide widening beyond the design specifications and enabling propagation of a higher-order TE mode.

Propagation losses in the fabricated waveguides were evaluated using the cutback method. The chips to be evaluated were half-cut on the back side, and the back side was then attached to a dicing tape and expanded to expose the chip end faces for optical coupling. In our optical evaluation setup, a 637-nm red light laser (Coherent OBIS LX FP) was used as the input light source. The laser was connected to a polarization-maintaining single-mode fiber (PM-S405-XP), and the lens tip at the end of the fiber was butt-coupled to the input end face of the chip. The light transmitted through the chip was collected by a lensed single-mode fiber (S405-XP) and its intensity was measured with a power meter (Thorlabs PM100D) connected to the fiber. To determine propagation loss, waveguide arrays of varying lengths (15–55 mm) were fabricated on multiple chips (~10 mm square) singulated from the same wafer. Each waveguide incorporated the same number of bends, with a bend radius of 120 μm to ensure that the bending losses were sufficiently small. Figure 2(b) shows the intensity plots of the transmitted optical power, normalized to the input power, as a function of waveguide length for TE or TM polarized input light. The propagation loss ranged from 2.30 to 4.52 dB/cm for the TE mode and 2.61–5.21 dB/cm for the TM mode, as determined by linear regression analysis of the individual chip data. The observed sample-to-sample variations in the optical propagation loss within the waveguides are attributed to non-uniform etching during ICP-RIE. While intra-chip variation was negligible, significant inter-chip variation resulted from a biased in-plane etching distribution.

To quantify sidewall roughness, focused ion beam-scanning electron microscopy (FIB-SEM) was employed on an un-embedded alumina waveguide fabricated under identical conditions to the embedded waveguide. To prevent the charge-up of SiO_2 and alumina during the SEM observation, a 7.5-nm-thick carbon coating was locally applied in advance. Figure 2(c) shows an SEM image of the waveguide sidewall, viewed parallel to the sidewall surface. Image processing of the SEM image, using contrast-based thresholding, allowed for the identification of the waveguide sidewalls (indicated by the red lines). Analysis of this profile yielded a root mean square (RMS) roughness σ of 3.0 nm and an autocorrelation length L_C of 27.7 nm. Substituting these parameters into an extended Payne–Lacey model for a three-dimensional channel waveguide[38,42] (using the average waveguide width), the scattering losses were calculated as 2.80 and 3.06 dB/cm for the TE and TM modes, respectively. The waveguide's top and bottom surface roughness were considered negligible and therefore excluded from the scattering loss estimation. Comparison with the experimental results suggests that scattering loss is the dominant contributor to propagation loss, highlighting the importance of suppressing sidewall roughness to reduce propagation loss. The finite-element method (FEM) simulations further reveal that the fundamental TM mode exhibits a stronger electromagnetic field distribution at the waveguide sidewalls, regions susceptible to sidewall roughness, compared to the fundamental TE mode (see appendix A). This increased field concentration in the TM mode leads to larger scattering losses, consistent with the experimentally observed higher propagation loss for the TM mode compared to the TE mode.[30]

Furthermore, we fabricated and evaluated alumina waveguides without SiO_2 PECVD embedding, which is advantageous for hybrid integration with other materials. The alumina layer was deposited using a different sputtering

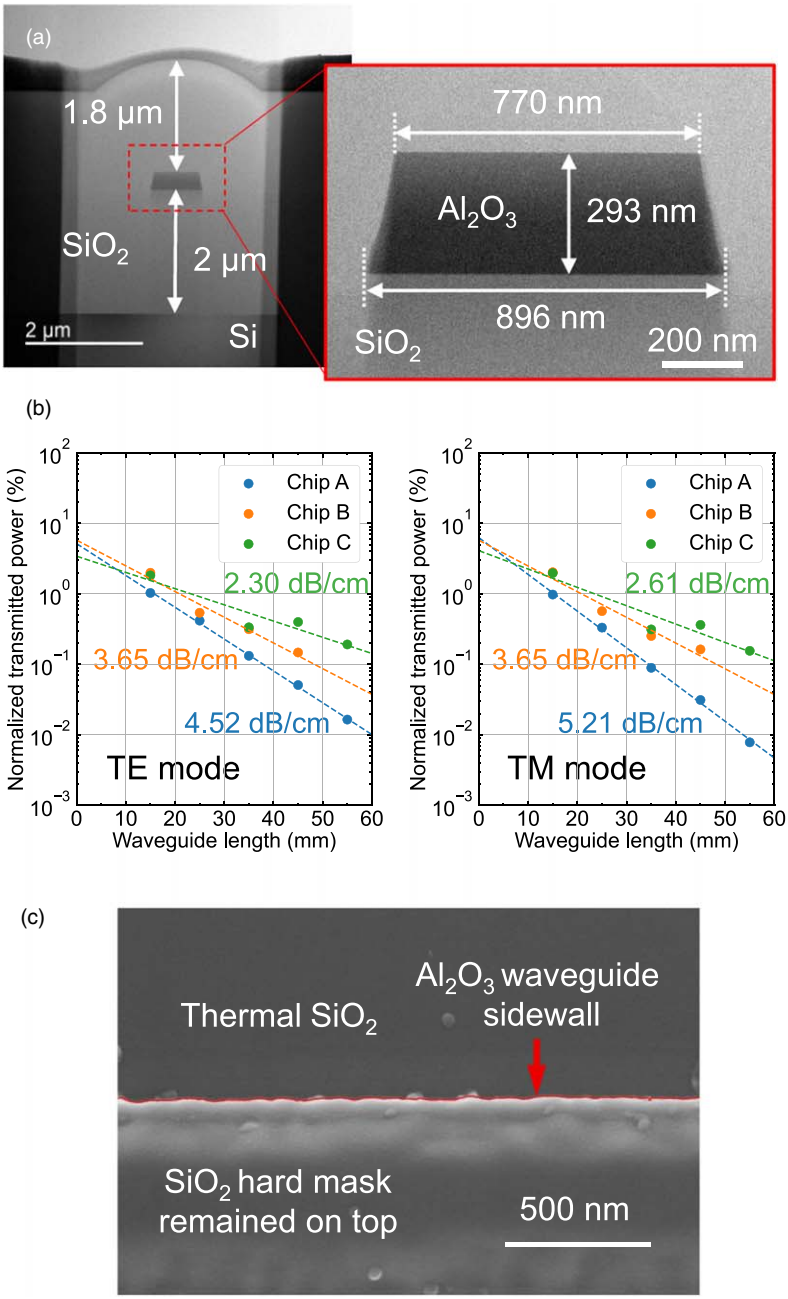

Fig. 2. (a) Cross-sectional bright-field transmission electron microscopy (TEM) image of an alumina waveguide embedded with a PECVD SiO_2 overcladding. (b) Optical characterization results under TE/TM incidence for three alumina waveguide chips embedded with PECVD SiO_2 overcladding. Missing data points are attributed to waveguide discontinuities and surface contamination. (c) SEM image (×150k) of the sidewall roughness of an unembedded alumina waveguide fabricated simultaneously and under identical conditions to the embedded waveguides, taken with the sample oriented parallel to the sidewall. A thin carbon film was coated onto the waveguide to prevent charge-up during observation (the granular structures are attributed to the carbon coating). The red lines indicate the waveguide sidewalls detected via image processing.

system than that used for the waveguide chips described previously, exhibiting a refractive index of 1.632 at 637 nm. In this study, we also employed a higher-resistance EB resist to improve the sidewall smoothness of the alumina waveguides. We designed the waveguides with three different widths, $W = 650$, 850, and 1050 nm. Previous experiments revealed significant waveguide broadening during RIE processes. Consequently, for waveguides fabricated without an overcladding, EB drawn widths were deliberately reduced to compensate for this effect. Hereafter, these dimensions will be referred to as the designed widths. Figure 3(a) shows a cross-sectional SEM image and corresponding scanning electron microscopy–energy dispersive X-ray (SEM-EDX) analysis of the widest waveguide. FEM calculations indicated that this waveguide geometry supports single-mode operation. Figure 3(b) shows the results of optical characterization under TE/TM incidence. The propagation loss (corresponding to the slope of the linear regression for each plot) tended to decrease with increasing waveguide width, likely due to the reduced impact of sidewall roughness. Specifically, a propagation loss of 1.39 dB/cm (TE mode) and 2.17 dB/cm (TM mode) was achieved for the waveguide with designed width $W = 1050$ nm, which is as low as those previously reported for non-embedded titanium oxide[17] and alumina waveguides[35] operating at the same red wavelength. Figure 3(c) shows SEM images of the waveguide sidewalls

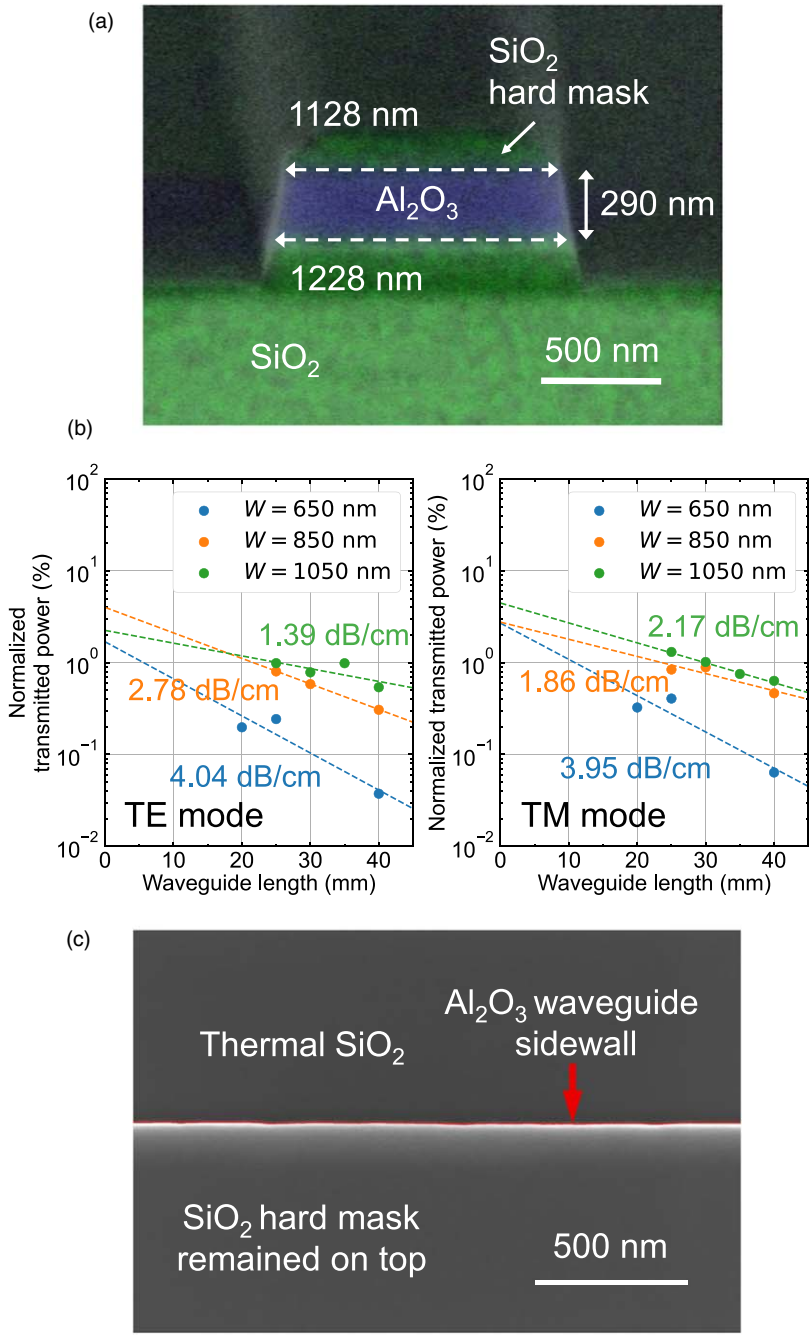

Fig. 3. (a) Cross-sectional SEM image overlaid with EDX elemental mapping of a fabricated unembedded alumina waveguide (designed waveguide width $W = 1050$ nm). (b) Optical characterization results under TE/TM incidence for unembedded alumina waveguide chips with designed waveguide widths W of 650, 850, and 1050 nm. Data points from defective waveguides have been excluded. (c) SEM image (×150k magnification) of the sidewall roughness of the alumina waveguide shown in (a). A thin carbon coating was applied beforehand to prevent charging during observation, which was performed parallel to the sidewall. The red lines indicate the waveguide sidewalls detected via image processing.

taken parallel to the sidewall direction. Compared to the results in Fig. 2(c), the sidewall roughness was significantly improved (RMS roughness $\sigma = 1.2$ nm, autocorrelation length $L_C = 60.9$ nm). SEM observation of the waveguide patterns after CCP-RIE etching of the SiO_2 hard mask reveals reduced roughness compared to the previous resist (see appendix B). This improvement is believed to have led to reduced roughness in the sidewalls of the alumina layer after subsequent ICP-RIE. Although the surface roughness of the SiO_2 layers was not included in the model, the calculated scattering losses attributable solely to the waveguide sidewalls were estimated to be 1.27 and 1.43 dB/cm for the TE and TM modes, respectively. This reduction in sidewall scattering loss is considered a contributing factor to the overall decrease in propagation loss.

3. Optical beam splitters

Next, we designed and fabricated directional coupler beam splitters based on unembedded alumina waveguides. A schematic of the beam splitter, showing the coupling length L and separation gap G between the two waveguides, is illustrated in Fig. 4(a). The upper and lower waveguides on both the left and right sides of the beam splitter have equal lengths. In our design, the coupling length L was set to 100 μm to achieve a 50:50 optical splitting ratio, even with a sufficiently wide separation gap to ensure proper device

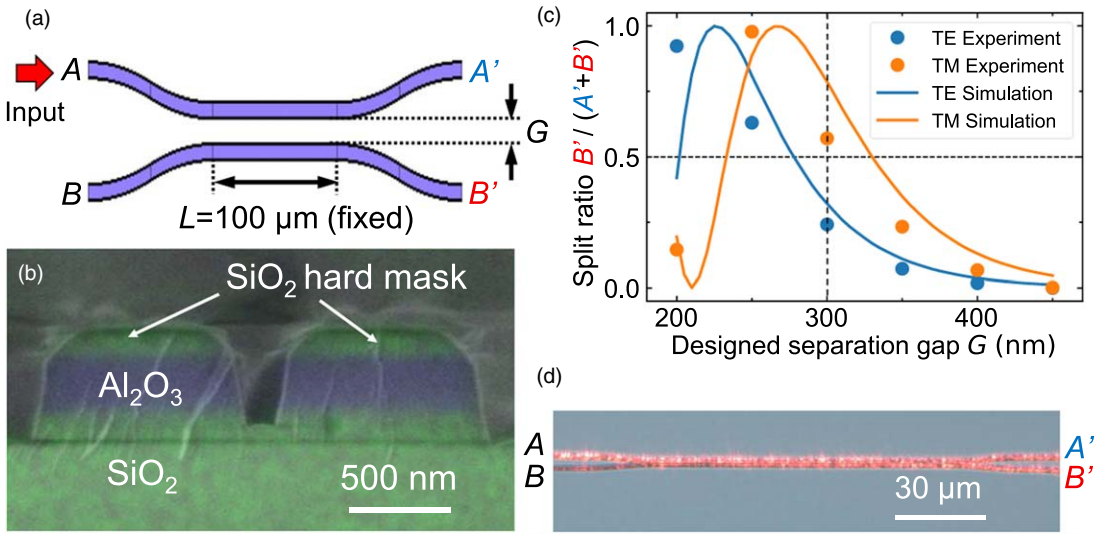

Fig. 4. (a) Schematic of a directional coupler beam splitter with a coupling length L and separation gap G between the waveguides. The upper and lower waveguides on both the left and right sides of the beam splitter have equal lengths. (b) Cross-sectional SEM image overlaid with EDX elemental mapping of the coupling region of a fabricated beam splitter with a designed waveguide width W of 850 nm and separation gap G of 300 nm. (c) Comparison of the experimental and numerical results for the optical splitting ratio of beam splitters fabricated with different designed gap widths for both TE and TM mode excitation. Numerical simulations were performed using the 3D-BPM method based on the waveguide geometry determined from SEM-EDX observations. (d) Experimental observation of light splitting (A': B' = 43: 57) at the beam splitter when TM-mode light is emitted from the upper-left port of a beam splitter fabricated with a designed gap G of 300 nm.

fabrication. This choice is compatible with the proposed architecture for scalable diamond NV-based quantum computers,[43] which utilizes a 1 mm spacing between unit cells to minimize crosstalk and requires only a few beam splitters per unit cell. A waveguide width of 850 nm was chosen to ensure single-mode operation, even considering potential broadening during fabrication. The devices were fabricated on substrates with a deposited alumina layer exhibiting a refractive index of 1.691 at 637 nm, utilizing the new EB resist described in the previous section, which demonstrated improved sidewall quality.

A cross-sectional SEM-EDX image of a fabricated beam splitter (designed separation gap $G = 300$ nm) is shown in Fig. 4(b). When the designed gap width was 200 nm or larger, two alumina waveguides could be fabricated without connecting to each other. During optical characterization, we emitted red light from the upper left port A. We then determined the optical splitting ratio defined as $B'/(A' + B')$, where A' and B' are the intensity of light emitted from the upper and lower right ports on the output side, respectively. Figure 4(c) compares the experimental results with numerical simulation results obtained using the three-dimensional beam propagation method (3D-BPM) based on the waveguide geometry identified from a cross-sectional SEM-EDX image. The results are shown for both TE and TM mode excitation. The discrepancy between the TE and TM mode plots stems from the difference in their effective refractive indices in the propagation modes. The experimental results are in good agreement with the numerical simulations, showing a trend of stronger optical coupling between the waveguides as they are brought closer together. These results demonstrate that the beam splitter's optical splitting ratio can be successfully tailored for both TE and TM modes by varying the waveguide separation gap G. In particular, a beam splitter with a design gap of 300 nm in the TM mode [Fig. 4(d)] achieved a splitting ratio suitable for practical application as a half beam splitter, indicating its potential utility for entangled photon-pair generation.

4. Conclusions

We fabricated visible light waveguides using aluminum oxide, a material exhibiting very low optical absorption in the visible spectrum. The fabricated unembedded waveguides, suitable for practical integration into hybrid structures with other materials, demonstrated minimal propagation losses of 1.39 and 2.17 dB/cm for the TE and TM modes, respectively, at a red-light wavelength of 637 nm. These low propagation loss values highlight the suitability of alumina as a superior material for visible light waveguides. Furthermore, we fabricated optical beam splitters based on these alumina waveguides and successfully demonstrated the tunability of the optical splitting ratio via design-parameter modification. This included the successful demonstration of a half beam splitter, which is essential for entangled photon generation. Our alumina waveguides and beam splitters represent a significant advancement toward the realization of visible-light-operation optical quantum chips, which are crucial for future quantum computing technologies.

Acknowledgments

This work was partially supported by "Advanced Research Infrastructure for Materials and Nanotechnology in Japan (ARIM)" of the Ministry of Education, Culture, Sports, Science and Technology (MEXT), proposal Numbers JPMXP1223NM0070 and JPMXP1224NM0089. We would like to thank Prof. Satoshi Iwamoto (The University of Tokyo) for the valuable discussions.

Appendix A: Electromagnetic field overlap at the sidewalls of SiO_2-embedded alumina waveguides

The measured propagation loss difference between TE and TM modes [Fig. 2(b)] is clarified by calculating the modal overlap

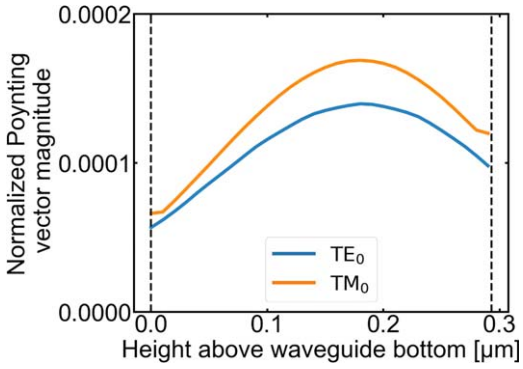

Fig. A·1. Normalized Poynting vector in the propagation direction at various heights along the sidewalls of the SiO_2-embedded alumina waveguide shown in Fig. 2(a). For each mode, values are normalized to its total in-plane power.

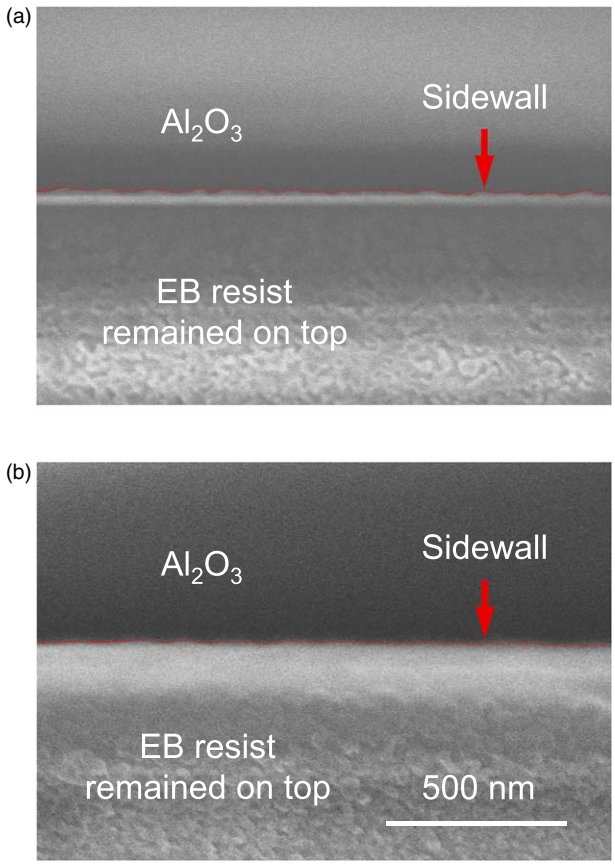

Fig. B·1. Top-down SEM images of waveguide patterns after SiO_2 hard mask etching by CCP-RIE using the EB resist (a) before and (b) after sidewall improvements. Red arrows indicate the sidewalls of the waveguide pattern.

with the sidewalls.[30] The fraction of total power interacting with the sidewalls is determined by integrating the Poynting vector in the propagation direction along the waveguide sidewalls and normalizing to the total in-plane power. Based on this concept, a FEM analysis was performed on the channel waveguide structure shown in Fig. 2(a). Figure A·1 depicts the variation of the normalized Poynting vector magnitude along the waveguide sidewall boundaries in the direction of the waveguide thickness. The mesh size used in the simulation (10 nm) was sufficiently small compared to the operating wavelength of 637 nm. First-order TE mode was considered negligible due to the waveguide structure's symmetry, and only the fundamental mode was considered. The simulation results reveal that, at all heights within the waveguide, the TM fundamental mode exhibits a larger power concentration near the sidewalls compared to the TE fundamental mode. The calculated ratio of the modal overlap with the sidewalls for TM and TE modes (obtained by integrating the normalized Poynting vector along the sidewalls) is 1.19. This result is in reasonable agreement with the calculated scattering loss ratio of 1.15 between TM and TE modes, obtained using the Payne–Lacey model (discussed in the main text). The larger sidewall overlap factor for the TM mode suggests a correspondingly larger scattering loss, ultimately resulting in the observed higher propagation loss. This calculated ratio shows good agreement with the experimentally measured ratios of TM to TE mode propagation loss shown in Fig. 2(b): 1.13 for Chip A, 1.00 for Chip B, and 1.15 for Chip C.

Appendix B: Sidewall roughness of waveguide patterns after SiO_2 hard mask etching

Employing each of the two EB resists (described in the main text) as etch masks, CCP-RIE processing of the SiO_2 hard mask yielded vertical sidewall profiles. To assess the impact of resist choice on sidewall roughness, a comparison of the hard mask profiles after dry etching was performed using top-down SEM observation. A comparison of the sidewall profiles after CCP-RIE etching of the SiO_2 hard mask reveals significant roughness with the former resist [Fig. B·1(a), RMS roughness $\sigma = 3.6$ nm, autocorrelation length $L_C = 20.4$ nm], while the latter resist exhibits considerably smoother sidewalls after CCP-RIE [Fig. B·1(b), RMS roughness $\sigma = 2.6$ nm, autocorrelation length $L_C = 36.6$ nm]. These sidewall profiles are believed to have been transferred to the alumina layer during subsequent ICP-RIE, thereby impacting waveguide propagation loss characteristics.

ORCID iDs

Takuto Yamaguchi https://orcid.org/0009-0001-7181-7101
Manabu Ohtomo https://orcid.org/0000-0001-8361-956X

1) M. A. Porcel, A. Hinojosa, H. Jans, A. Stassen, J. Goyvaerts, D. Geuzebroek, M. Geiselmann, C. Dominguez, and I. Artundo, Opt. Laser Technol. **112**, 299 (2019).
2) A. Mohanty et al., Nat. Biomed. Eng. **4**, 223 (2020).
3) D. Kohler, G. Schindler, L. Hahn, J. Milvich, A. Hofmann, K. Länge, W. Freude, and C. Koos, Light: Sci. Appl. **10**, 64 (2021).
4) M. Raval, A. Yaacobi, and M. R. Watts, Opt. Lett. **43**, 3678 (2018).
5) M. C. Shin et al., Opt. Lett. **45**, 1934 (2020).
6) H. Choi, M. Pant, S. Guha, and D. Englund, npj Q. Inform. **5**, 104 (2019).
7) M. H. Abobeih, Y. Wang, J. Randall, S. J. H. Loenen, C. E. Bradley, M. Markham, D. J. Twitchen, B. M. Terhal, and T. H. Taminiau, Nature **606**, 884 (2022).
8) R. Ishihara et al., IITC/MAM2023p. 10.4.
9) R. J. Niffenegger et al., Nature **586**, 538 (2020).
10) M. Pompili et al., Science **372**, 259 (2021).
11) C. Xiong, W. H. P. Pernice, X. Sun, C. Schuck, K. Y. Fong, and H. X. Tang, New J. Phys. **14**, 095014 (2012).
12) M. Stegmaier, J. Ebert, J. M. Meckbach, K. Ilin, M. Siegel, and W. H. P. Pernice, Appl. Phys. Lett. **104**, 091108 (2014).
13) T-J. Lu et al., Opt. Express **26**, 11147 (2018).
14) X. Liu, A. W. Bruch, Z. Gong, J. Lu, J. B. Surya, L. Zhang, J. Wang, J. Yan, and H. X. Tang, Optica **5**, 1279 (2018).
15) M. Furuhashi, M. Fujiwara, T. Ohshiro, M. Tsutsui, K. Matsubara, M. Taniguchi, S. Takeuchi, and T. Kawai, AIP Adv. **1**, 032102 (2011).
16) J. T. Choy, J. D. B. Bradley, P. B. Deotare, I. B. Burgess, C. C. Evans, E. Mazur, and M. Lončar, Opt. Lett. **37**, 539 (2012).

17) C. C. Evans, C. Liu, and J. Suntivich, Opt. Express **23**, 11160 (2015).
18) I. Hegeman, M. Dijkstra, and S. M. García-Blanco, Integr. Opt. Devices Mater. Technol. XXIV **11283**, 23 (2020).
19) S. M. Lindecrantz and O. G. Hellesø, IEEE Photon. Technol. Lett. **26**, 1836 (2014).
20) Y-Y. Lin, C-L. Wu, W-C. Chi, Y-J. Chiu, Y-J. Hung, A-K. Chu, and C-K. Lee, Opt. Express **24**, 21633 (2016).
21) J. H. Sierra, R. C. Rangel, R. E. Samad, N. D. Vieira, M. I. Alayo, and D. O. Carvalho, Opt. Express **27**, 37516 (2019).
22) C. Sorace-Agaskar, D. Kharas, S. Yegnanarayanan, R. T. Maxson, G. N. West, and W. Loh, IEEE J. Select. Top. Quantum Electron. **25**, 1 (2019).
23) S. Romero-García, F. Merget, F. Zhong, H. Finkelstein, and J. Witzens, Opt. Express **21**, 14036 (2013).
24) A. Z. Subramanian, P. Neutens, A. Dhakal, R. Jansen, T. Claes, and X. Rottenberg, IEEE Photon. J. **5**, 2202809 (2013).
25) E. Shim, Y. Chen, S. Masmanidis, and M. Li, Sci. Rep. **6**, 22693 (2016).
26) W. D. Sacher et al., Opt. Express **27**, 37400 (2019).
27) T. J. Morin, L. Chang, W. Jin, C. Li, J. Guo, H. Park, M. A. Tran, T. Komljenovic, and J. E. Bowers, Optica **8**, 755 (2021).
28) N. Chauhan, J. Wang, D. Bose, K. Liu, R. L. Compton, C. Fertig, C. W. Hoyt, and D. J. Blumenthal, Opt. Express **30**, 6960 (2022).
29) M. Lelit et al., Materials **15**, 1398 (2022).
30) M. Corato-Zanarella, X. Ji, A. Mohanty, and M. Lipson, Opt. Express **32**, 5718 (2024).
31) B. Desiatov, A. Shams-Ansari, M. Zhang, C. Wang, and M. Lončar, Optica **6**, 380 (2019).
32) G. N. West, W. Loh, D. Kharas, C. Sorace-Agaskar, K. K. Mehta, J. Sage, J. Chiaverini, and R. J. Ram, APL Photonics **4**, 026101 (2019).
33) C. Lin, J. S. D. Peñaranda, J. Dendooven, C. Detavernier, D. Schaubroeck, N. Boon, R. Baets, and N. L. Thomas, Nat. Commun. **13**, 4360 (2022).
34) C. He, Y. Wang, C. Waldfried, G. Yang, J-F. Zheng, S. Hu, and H. X. Tang, Opt. Express **31**, 33923 (2023).
35) E. McKay, N. G. Pruiti, S. May, and M. Sorel, Sci. Rep. **13**, 19917 (2023).
36) W. A. Hendriks, D. B. Bonneville, S. Mardani, M. Dijkstra, and S. M. Garcia-Blanco, Opt. Open (2024), UV integrated photonics in sputter deposited aluminum oxide.
37) G. Jeevanandam, N. P. Pham, E. Mafakheri, E. Vecchio, D. C. Altamirano, V. Prakasam, Z. Jafari, C. Haffner, and P. Helin, Ext. Abstr. of Int. Conf. on Solid State Devices and Materials (SSDM), E-4-03, 2024.
38) F. P. Payne and J. P. R. Lacey, Opt. Quantum Electron. **26**, 977 (1994).
39) E. O. Filatova and A. S. Konashuk, J. Phys. Chem. C **119**, 20755 (2015).
40) S. Tegenz and P. Moll, J. Electrochem. Soc. **152**, G271 (2005).
41) T. Yamaguchi, N. Fushimi, M. Ohtomo, T. Miyatake, S. Miyahara, H. Hosoi, T. Miyazawa, K. Kawaguchi, R. Ishihara, and S. Sato, Ext. Abstr. of Int. Conf. on Solid State Devices and Materials (SSDM), E-4-04, 2024.
42) K. P. Yap, A. Delage, J. Lapointe, B. Lamontagne, J. H. Schmid, and P. Waldron, J. Light. Technol. **27**, 3999 (2009).
43) N. Fakkel et al., IEEE J. Solid-State Circuits **59**, 3627 (2024).